

Quarkonium states in a complex-valued potential

Matthew Margotta, Kyle McCarty, Christina McGahan,
Michael Strickland, and David Yager-Elorriaga

*Department of Physics, Gettysburg College,
Gettysburg, PA 17325, USA*

Abstract

We calculate quarkonium binding energies using a realistic complex-valued potential for both an isotropic and anisotropic quark-gluon plasma. We determine the disassociation temperatures of the ground and first excited states considering both the real and imaginary parts of the binding energy. We show that the effect of momentum-space anisotropy is smaller on the imaginary part of the binding energy than on the real part of the binding energy. In the case that one assumes an isotropic plasma, we find disassociation temperatures for the J/ψ , Υ and χ_b of $1.6 T_c$, $2.8 T_c$, and $1.5 T_c$, respectively. We find that a finite oblate momentum-space anisotropy increases the disassociation temperature for all states considered and results in a splitting of the p-wave states associated with the χ_b first excited state of bottomonium.

I. INTRODUCTION

The behavior of nuclear matter at extreme temperatures is now being studied with the highest collision energies ever achieved using the Large Hadron Collider (LHC) at CERN. The ultrarelativistic heavy ion collisions being studied there will eventually have a center of mass energy of 5.5 TeV per nucleon, which is 27.5 times higher than the 200 GeV per nucleon energy achieved at the Relativistic Heavy Ion Collider (RHIC) at Brookhaven National Laboratory. At RHIC, observations indicated that initial temperatures on the order of twice the critical temperature for the quark-gluon plasma phase transition were generated. This corresponds to $T_0 \sim 360$ MeV. Assuming that the initial temperature scales with the fourth root of the collision energy as predicted by dimensional analysis, one predicts that initial temperatures on the order of $T_0 \sim 4.6 T_c \sim 830$ MeV will be generated at the LHC. At such high temperatures, one expects to generate a quark-gluon plasma in which the formation of quark bound states is suppressed in favor of a state of matter consisting of a deconfined plasma of quarks and gluons.

Suppression of quark bound states follows from the fact that in the quark-gluon plasma one expects color charge to be Debye screened [1, 2]. This effect led to early proposals to use heavy quarkonium production to measure the temperature of the quark-gluon plasma. Heavy quarkonium has received the most theoretical attention since heavy quark states are dominated by short rather than long distance physics at low temperatures and can be treated using heavy quark effective theory. Based on such effective theories of Quantum Chromodynamics (QCD) with weak coupling at short distances, non-relativistic quarkonium states can be reliably described. Their binding energies are much smaller than the quark mass $m_Q \gg \Lambda_{\text{QCD}}$ ($Q = c, b$), and their sizes are much larger than $1/m_Q$. At zero temperature, since the velocity of the quarks in the bound state is small, $v \ll c$, quarkonium can be understood in terms of non-relativistic potential models [3] such as the Cornell potential [4]. Such potential models can be derived directly from QCD as an effective field theory (potential non-relativistic QCD - pNRQCD) by integrating out modes above the scales m_Q and then $m_Q v$, respectively [5].

As mentioned above, at high temperature the deconfined phase of QCD exhibits screening of static color-electric fields. It is expected that this screening leads to the dissociation of quarkonium states, which can serve as a signal for the formation of a deconfined quark-gluon plasma in heavy ion collisions [6]. Inspired by the success at zero temperature, potential model descriptions have also been applied to understand quarkonium properties at finite temperature. The pioneering paper of Matsui and Satz [6] was followed by the work of Karsch, Mehr, and Satz [7], which presented the first quantitative calculation of quarkonium properties at high temperature. In recent work, more involved calculations of quarkonium spectral functions and meson current correlators obtained from potential models have been performed [8–15]. The results have been compared to first-principle QCD calculations performed numerically on lattices [16–24] which rely on the maximum entropy method [25–27].

A summary and review of the current understanding of potential models is presented in [15], and different aspects of quarkonium in collider experiments can be found in [28, 29]. In recent years, the imaginary part of the potential due to Landau damping has been calculated [30–32]. Also, the derivation of potential models from QCD via effective field theory methods has been extended to finite temperature [33]. All of the aforementioned calculations, however, were performed with the assumption of an isotropic thermal medium.

In the last few years there has been an interest in the effect of plasma momentum-space anisotropies on quarkonium binding energies for both ground and excited states [34–39]. The interest stems from the fact that at early times a viscous quark-gluon plasma can have large momentum-space anisotropies [40–48]. Depending on the magnitude of the shear viscosity, these momentum-space anisotropies can persist for a long time ($\sim 1 - 10$ fm/c). The first paper to consider the quarkonium potential in a momentum-space anisotropic plasma [34] considered only the real part of the potential; however, two recent works have extended the calculation to include the imaginary part of the potential [36, 37]. In this paper we use the imaginary part of the potential derived in [37] and include it in a phenomenological model of the heavy quarkonium potential. We then numerically solve the three-dimensional Schrödinger equation to find the real and imaginary parts of the binding energies and full quantum wavefunctions of the charmonium and bottomonium ground states, as well as the first excited state of bottomonium. We present data as a function of the temperature and are able to identify the full effect of the isotropic and anisotropic potentials on these states.

We compare our results with a recent analytic estimate of the imaginary part of the binding energy by Dumitru [49]. We show that, for an isotropic plasma, the imaginary part of the binding energy is approximately linear in the temperature for temperatures near the phase transition in agreement with Ref. [49]. However, in the case of the J/ψ , we find a significantly smaller slope for the imaginary part of the binding energy as a function of temperature than predicted by Ref. [49]. The discrepancy most likely arises from the fact that Ref. [49] assumed Coulombic wavefunctions. The potential used here includes modifications at both intermediate and long ranges, which causes the numerical wavefunctions to not be well approximated by Coulombic wavefunctions. In addition, our wavefunctions are complex with the imaginary part growing in magnitude as the temperature is increased. This effect was ignored by the assumption of Coulombic wavefunctions in Ref. [49]. We find that when the states are small and dominated by the screened Coulomb potential, the imaginary part of the binding energy increases approximately linearly with the temperature; however, as the size of the bound state increases, the scale set by the string tension dominates and the imaginary part of the binding energy increases more slowly with increasing temperature.

The structure of this paper is as follows: In Sec. II, we review the potential introduced in Ref. [35] and extend it to include the imaginary part of the potential derived in Ref. [37]. In Sec. III, we review the numerical method that we use to solve the three-dimensional Schrödinger equation. In Sec. IV, we present our numerical results for the real and imaginary parts of the binding energies of the charmonium and bottomonium ground states and first excited state of bottomonium. In Sec. V, we state our conclusions and give an outlook for future work. Finally, in an appendix we present numerical benchmarks and tests of the code used here in order to demonstrate its convergence and applicability to the problem at hand.

II. SETUP AND MODEL POTENTIAL

In this section we specify the potential we use in this work. We consider the general case of a quark-gluon plasma which is anisotropic in momentum space. In the limit that the plasma is assumed to be isotropic, the real part of the potential used here reduces to the model originally introduced by Karsch, Mehr, and Satz (KMS) [7] with an additional entropy contribution [35] and the imaginary part reduces to the result originally obtained by Laine et al [30]. To begin the discussion we first introduce our ansatz for the one-particle

distribution function subject to a momentum-space anisotropy.

A. The anisotropic plasma

The phase-space distribution of gluons in the local rest frame is assumed to be given by the following ansatz [34, 50–53]

$$f(\mathbf{x}, \mathbf{p}) = f_{\text{iso}} \left(\sqrt{\mathbf{p}^2 + \xi(\mathbf{p} \cdot \mathbf{n})^2} / p_{\text{hard}}^2 \right), \quad (1)$$

where p_{hard} is a scale which specifies the typical momentum of the particles in the plasma and can be identified with the temperature in the limit that $\xi = 0$. Thus, $f(\mathbf{x}, \mathbf{p})$ is obtained from an isotropic distribution $f_{\text{iso}}(|\mathbf{p}|)$ by removing particles with a large momentum component along \mathbf{n} , the direction of anisotropy. In this paper, we will restrict our consideration to a plasma that is close to equilibrium. This is motivated by the fact that in a heavy-ion collision, quarkonium states are expected to form when the temperature has dropped to (1-2) T_c . At such temperatures the plasma may have partly equilibrated/isotropized. Additionally, this means that we can assume that the function $f_{\text{iso}}(|\mathbf{p}|)$ is a thermal distribution function.

The parameter ξ determines the degree of anisotropy,

$$\xi = \frac{1}{2} \frac{\langle \mathbf{p}_{\perp}^2 \rangle}{\langle p_z^2 \rangle} - 1, \quad (2)$$

where $p_z \equiv \mathbf{p} \cdot \mathbf{n}$ and $\mathbf{p}_{\perp} \equiv \mathbf{p} - \mathbf{n}(\mathbf{p} \cdot \mathbf{n})$ denote the particle momentum along and perpendicular to the direction \mathbf{n} of anisotropy, respectively. If ξ is small, then it is also related to the shear viscosity of the plasma. For example, for one-dimensional boost-invariant expansion governed by Navier-Stokes evolution [45, 47, 48, 54] one finds

$$\xi = \frac{10}{T\tau} \frac{\eta}{s}, \quad (3)$$

where T is the temperature, τ is the proper time (and $1/\tau$ is the Hubble expansion rate), and η/s is the ratio of shear viscosity to entropy density. In an expanding system, non-vanishing viscosity (finite momentum relaxation rate) implies an anisotropy of the particle momenta which increases with the expansion rate $1/\tau$. For $\eta/s \simeq 0.1 - 0.2$ and $\tau T \simeq 1 - 3$ one finds that $\xi \simeq 1$. In general, one can relate ξ to the longitudinal and transverse pressures in the plasma and it is possible to derive dynamical differential equations which govern its time evolution similar to viscous hydrodynamics [47, 48]

We point out that in this paper we restrict ourselves to solving the time-independent Schrödinger equation, i.e. we assume that the plasma is at a constant hard momentum scale p_{hard} and anisotropy ξ . This approximation is useful if the time scale associated with the bound state, $\sim 1/|E_{\text{bind}}|$, is short compared to the time scales over which p_{hard} and ξ vary. Indeed, for sufficiently large quark mass m_Q this condition should be satisfied.

B. The model potential

Lacking knowledge of the exact heavy-quark potential at finite temperature, different phenomenological potentials and lattice-QCD based potentials have been used to study

quarkonium binding energies in the quark-gluon plasma. To start, we decompose the potential into real and imaginary parts, $V = V_R + iV_I$. The model for the real part of the potential we use was obtained in Ref. [35]. The analytic calculation of the imaginary part was performed in Refs. [30, 37, 55]. The real part is given by

$$V_R(\mathbf{r}) = -\frac{\alpha}{r} (1 + \mu r) \exp(-\mu r) + \frac{2\sigma}{\mu} [1 - \exp(-\mu r)] - \sigma r \exp(-\mu r) - \frac{0.8 \sigma}{m_Q^2 r}, \quad (4)$$

where

$$\frac{\mu}{m_D} \equiv 1 - \xi \frac{3 + \cos 2\theta}{16}, \quad (5)$$

with $m_D = (1.4)^2 \cdot N_c(1 + N_f/6) 4\pi\alpha_s p_{\text{hard}}^2/3$ being the isotropic leading-order Debye mass adjusted by a factor of $(1.4)^2$ to take into account higher-order corrections [56]. The coupling α folds in a factor of $C_F = (N_c^2 - 1)/(2N_c)$, i.e. $\alpha \equiv C_F\alpha_s$, where $\alpha_s = g_s^2/(4\pi)$ is the canonically defined strong coupling constant. We have taken $N_c = 3$ and assumed $N_f = 2$ which is appropriate for the temperature range considered herein. The first term in (4) is a screened Coulomb potential with an entropy addition. The second and third terms are a screened linear potential associated with confinement in the low temperature limit. The last term in (4) is a relativistic correction which is critical for obtaining accurate binding energies in the low temperature limit. For the string tension, we fix $\sigma = 0.223$ GeV and for the strong coupling constant we fix $\alpha = 0.385$.¹

The imaginary part is given by [37]

$$V_I(\mathbf{r}) = -\alpha T \left[\phi(\hat{r}) - \xi (\psi_1(\hat{r}, \theta) + \psi_2(\hat{r}, \theta)) \right], \quad (6)$$

where $\hat{r} = m_D r$ and

$$\phi(\hat{r}) = 2 \int_0^\infty dz \frac{z}{(z^2 + 1)^2} \left[1 - \frac{\sin(z\hat{r})}{z\hat{r}} \right], \quad (7)$$

$$\psi_1(\hat{r}, \theta) = \int_0^\infty dz \frac{z}{(z^2 + 1)^2} \left(1 - \frac{3}{2} \left[\sin^2 \theta \frac{\sin(z\hat{r})}{z\hat{r}} + (1 - 3 \cos^2 \theta) G(\hat{r}, z) \right] \right), \quad (8)$$

$$\psi_2(\hat{r}, \theta) = - \int_0^\infty dz \frac{\frac{4}{3}z}{(z^2 + 1)^3} \left(1 - 3 \left[\left(\frac{2}{3} - \cos^2 \theta \right) \frac{\sin(z\hat{r})}{z\hat{r}} + (1 - 3 \cos^2 \theta) G(\hat{r}, z) \right] \right), \quad (9)$$

with θ being the angle from the beam direction and

$$G(\hat{r}, z) = \frac{\hat{r}z \cos(\hat{r}z) - \sin(\hat{r}z)}{(\hat{r}z)^3}. \quad (10)$$

The short range part of V_R is based on a leading order hard-loop perturbation theory calculation presented in Ref. [34]. V_I is also obtained from a leading order perturbative calculation [37]. Being a leading order calculation one may wonder about higher order

¹ Since α_s runs logarithmically and therefore has small variation in the temperature ranges shown, we will ignore the running of the coupling here. Incorporating this effect would be straightforward, however, a model of the behavior of α_s at large scales would be required in order fit zero temperature properties of the states considered here.

corrections. One expects that the leading order calculation pQCD would receive large corrections at low temperatures ($T < 10 T_c$) since the running coupling becomes large ($g_s > 1$). For the coupling used above $\alpha_s = 0.29$ one finds $g_s = \sqrt{4\pi\alpha_s} = 1.9$. This means that the normal scale hierarchy, $g_s T < T$, implicit in the hard-loop resummation becomes inverted.² We therefore need to supplement the leading order pQCD calculation with a non-perturbative contribution. For the real part we do this by including a long-range screened linear contribution that is modified to include an entropy contribution [34]. In the isotropic limit the resulting form of the real part potential is in good agreement with lattice data for the heavy quark potential [56]. For the imaginary part we currently do not have non-perturbative input from lattice calculations with which to constrain the long range part; however, we note that calculations of the real and imaginary parts of the potential using the AdS/CFT correspondence to calculate the corresponding potential in large t' Hooft coupling limit of $\mathcal{N} = 4$ Supersymmetric Yang-Mills yield similar results to those obtained using perturbative QCD [38, 61]. For more information about the relevant scales and limitations of the current approach we refer the reader to Sec. III of Ref. [34].

Regarding the length scales which are relevant, we note that the short range part of the potential is appropriate for describing wavefunctions which have $1/\langle r \rangle < \mathcal{O}(m_D)$ while the long range part is relevant if $1/\langle r \rangle > \mathcal{O}(m_D)$. Using the form of the real potential listed above, one finds that the distance scale at which medium effects become large is roughly given by $r > r_{\text{med}} \sim T_c/(2T)$ fm corresponding to $r_{\text{med}} \sim 0.25$ fm at $2 T_c$ [34]. Numerically, the isotropic Debye mass used herein is $m_D \sim 3p_{\text{hard}}$, corresponding to $m_D \sim 1.2$ GeV at $p_{\text{hard}} = 2T_c$. As shown in Ref. [34] Fig. 4, using the real part of the potential listed above, the RMS radius of the J/Ψ state is approximately 0.8 fm at $2 T_c$ corresponding to $1/\langle r \rangle \sim 250$ MeV, which makes the screening of the long range part of the potential crucially important for fixing the binding energy in this case. For the case of the Υ one sees also from Ref. [34] Fig. 4 that the RMS radius of the Υ is approximately 0.25 fm corresponding to $1/\langle r \rangle \sim 800$ MeV. We note importantly that for the Υ , due to its relatively small size, the bulk of the medium effect comes from the temperature dependence of $\lim_{r \rightarrow \infty} V \equiv V_\infty$ (see Fig. 3 of Ref. [34]). In closing, one finds that for both the J/Ψ and Υ that correct modeling of both the short and long range parts of the potential are critical for obtaining the temperature dependence of these states. As mentioned above, here we extend the results in [34] to include the imaginary part of the potential. We note that one finds that RMS radii of the states are only weakly affected by inclusion of the imaginary part of the potential, allowing us to use the estimates above as a rough guide for understanding the relevant scales.

C. Analytic estimate in isotropic case

In a recent paper [49], Dumitru made an estimate of the effect of the imaginary part of the potential on the imaginary part of the binding energy of a quarkonium state. For this estimate Dumitru assumed a Coulomb wavefunction for the quarkonium state and computed the expectation value of the imaginary part of the potential exactly in the case of an isotropic

² We note that for temperatures $T > 2 T_c$ NNLO perturbative calculations of QCD thermodynamics based on hard-thermal-loop resummation of QCD agree quite well with available lattice data even though g_s is large [57–60].

plasma. The result obtained was

$$\Gamma(\xi = 0) = \frac{T m_D^2}{\alpha m_Q^2} \frac{1 - (2 - \kappa^2)^2 + 4 \log \frac{1}{\kappa}}{(1 - \kappa^2)^3} , \quad \kappa = \frac{1 m_D}{\alpha m_Q} . \quad (11)$$

When plotted in the temperature range between T_c and $3T_c$ the result above is approximately linear for both the J/ψ and Υ [49]. For charmonium with $m_Q = 1.3$ GeV and using the values given for α and m_D in the previous subsection, we obtain a slope consistent with $\Gamma \propto (0.08 \text{ GeV}) T/T_c$ at $T = 0.3$ GeV. Similarly, for bottomonium with $m_Q = 4.7$ GeV we obtain a slope consistent with $\Gamma \propto (0.05 \text{ GeV}) T/T_c$. We note these here for later comparison with numerical results presented in the results section.

III. NUMERICAL METHOD

To determine the wavefunctions of bound quarkonium states, we solve the Schrödinger equation

$$\begin{aligned} \hat{H} \phi_v(\mathbf{x}) &= E_v \phi_v(\mathbf{x}) , \\ \hat{H} &= -\frac{\nabla^2}{2m_R} + V(\mathbf{x}) + m_1 + m_2 , \end{aligned} \quad (12)$$

on a three-dimensional lattice in coordinate space with the potential given by $V = V_R + iV_I$ where the real and imaginary parts are specified in Eqs. (4) and (6), respectively. Here, m_1 and m_2 are the masses of the two heavy quarks and m_R is the reduced mass, $m_R = m_1 m_2 / (m_1 + m_2)$. The index v on the eigenfunctions, ϕ_v , and energies, E_v , represents a list of all relevant quantum numbers, such as n , l , and m for a radial Coulomb potential. Due to the anisotropic screening scale, the wavefunctions are no longer radially symmetric if $\xi \neq 0$. Since we consider only small anisotropies we nevertheless label the states as $1S$ (ground state) and $1P$ (first excited state), respectively.

To find solutions to Eq. (12), we use the finite difference time domain method (FDTD) [62, 63]. In this method we start with the time-dependent Schrödinger equation

$$i \frac{\partial}{\partial t} \psi(\mathbf{x}, t) = \hat{H} \psi(\mathbf{x}, t) , \quad (13)$$

which can be solved by expanding in terms of the eigenfunctions, ϕ_v :

$$\psi(\mathbf{x}, t) = \sum_v c_v \phi_v(\mathbf{x}) e^{-iE_v t} . \quad (14)$$

If one is only interested in the lowest energy states (ground state and first few excited states) an efficient way to proceed is to transform (13) and (14) to Euclidean time using a Wick rotation, $\tau \equiv it$:

$$\frac{\partial}{\partial \tau} \psi(\mathbf{x}, \tau) = -\hat{H} \psi(\mathbf{x}, \tau) , \quad (15)$$

and

$$\psi(\mathbf{x}, \tau) = \sum_v c_v \phi_v(\mathbf{x}) e^{-E_v \tau} . \quad (16)$$

For details of the discretizations used etc. we refer the reader to Refs. [62, 63].

A. Finding the ground state

By definition, the ground state is the state with the lowest energy eigenvalue, E_0 . Therefore, at late imaginary time the sum over eigenfunctions (16) is dominated by the ground state eigenfunction

$$\lim_{\tau \rightarrow \infty} \psi(\mathbf{x}, \tau) \rightarrow c_0 \phi_0(\mathbf{x}) e^{-E_0 \tau} . \quad (17)$$

Due to this, one can obtain the ground state wavefunction, ϕ_0 , and energy, E_0 , by solving Eq. (15) starting from a random three-dimensional wavefunction, $\psi_{\text{initial}}(\mathbf{x}, 0)$, and evolving forward in imaginary time. This initial wavefunction should have a nonzero overlap with all eigenfunctions of the Hamiltonian; however, due to the damping of higher-energy eigenfunctions at sufficiently late imaginary times we are left with only the ground state, $\phi_0(\mathbf{x})$. Once the ground state wavefunction (or any other wavefunction) is found, we can compute its energy eigenvalue via

$$E_v(\tau \rightarrow \infty) = \frac{\langle \phi_v | \hat{H} | \phi_v \rangle}{\langle \phi_v | \phi_v \rangle} = \frac{\int d^3 \mathbf{x} \phi_v^* \hat{H} \phi_v}{\int d^3 \mathbf{x} \phi_v^* \phi_v} . \quad (18)$$

To obtain the binding energy of a state, $E_{v,\text{bind}}$, we subtract the quark masses and the real part of the potential at infinity

$$E_{v,\text{bind}} \equiv E_v - m_1 - m_2 - \frac{\langle \phi_v | \text{Re}[V(\theta, |\mathbf{r}| \rightarrow \infty)] | \phi_v \rangle}{\langle \phi_v | \phi_v \rangle} . \quad (19)$$

For the isotropic KMS potential the last term is independent of the quantum numbers v and equal to $2\sigma/m_D$. In the anisotropic case, however, this is no longer true since the operator $V_\infty(\theta)$ carries angular dependence, as discussed above. Its expectation value is, of course, independent of θ but does depend on the anisotropy parameter ξ .

B. Finding the excited states

The basic method for finding excited states is to first evolve the initially random wavefunction to large imaginary times, find the ground state wavefunction, ϕ_0 , and then project this state out from the initial wavefunction and re-evolve the partial-differential equation in imaginary time. However, there are (at least) two more efficient ways to accomplish this. The first is to record snapshots of the 3d wavefunction at a specified interval τ_{snapshot} during a single evolution in τ . After having obtained the ground state wavefunction, one can go back and extract the excited states by projecting out the ground state wavefunction from the recorded snapshots of $\psi(\mathbf{x}, \tau)$.

An alternative way to select different excited states is to impose a symmetry condition on the initially random wavefunction which cannot be broken by the Hamiltonian evolution. For example, one can select the first excited state of the (anisotropic) potential by antisymmetrizing the initial wavefunction around either the x , y , or z axes. In the anisotropic case this trick can be used to separate the different polarizations of the first excited state of the quarkonium system and to determine their energy eigenvalues with high precision. This high precision allows one to more accurately determine the splitting between polarization states which are otherwise degenerate in the isotropic Debye-Coulomb potential.

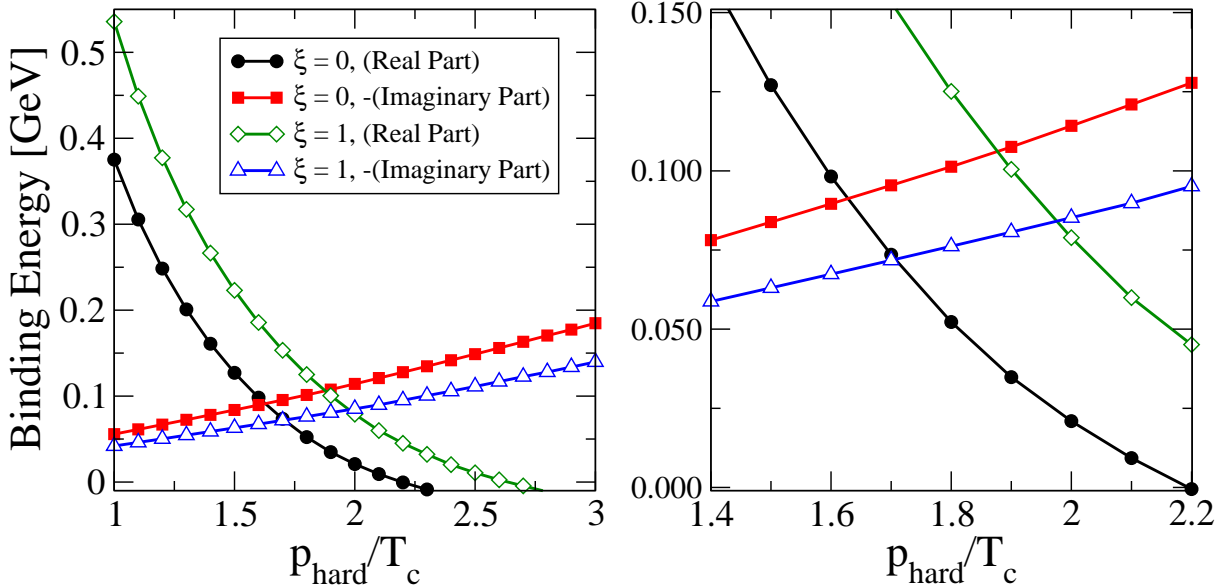


FIG. 1: Real and imaginary parts of the charmonium ground state (J/ψ) binding energy as a function of p_{hard} . Both isotropic $\xi = 0$ and anisotropic $\xi = 1$ cases are shown. The left panel shows full temperature range and the right panel focuses on the region where the real and imaginary parts become comparable. See text for parameters such as lattice size, lattice spacing, etc.

Whichever method is used, once the wavefunction of an excited state has been determined one can again use the general formulas (18) and (19) to determine the excited state binding energy. For code benchmarks and tests see App. A.

IV. RESULTS AND DISCUSSION

In this section we present results for isotropic ($\xi = 0$) and anisotropic ($\xi = 1$) binding energies for charmonium (J/ψ), bottomonium (Υ), and the first excited state of bottomonium (χ_b) as a function of the hard momentum scale p_{hard} . We will first assume that p_{hard} is held constant and vary the anisotropy parameter. Note increasing ξ results in a decrease in the density since $n \propto p_{\text{hard}}^3/\sqrt{1+\xi}$ [34]. This reduced density results in less Debye screening and thus a more strongly bound state. We therefore expect that states with large anisotropy will have increased binding energies compared to the isotropic states. One could imagine holding another thermodynamic property such as the number density or energy density constant as one changes the anisotropy parameter. We will return to this issue at the end of this section and show that the results in these cases can be obtained from a simple rescaling of the results presented below. In all plots shown, we assume $T_c = 192$ MeV and fix the imaginary-time step in the numerical algorithm to be $\Delta\tau = a^2/8$ where a is the spatial lattice spacing.

A. Results as a function of the hard momentum scale

In Fig. 1 we plot the binding energy of the charmonium ground state (J/ψ) as a function of p_{hard} . For this figure, we used a lattice size of 256^3 with lattice dimension of $L = 25.6$ GeV $^{-1}$ and a lattice spacing of $a = 0.1$ GeV $^{-1}$. For the charmonium mass, we used $m_c = 1.3$

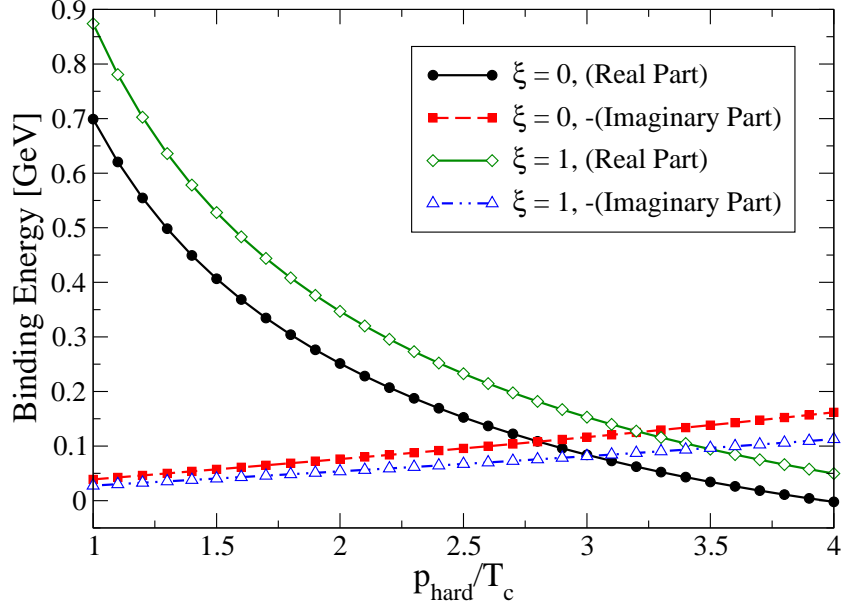


FIG. 2: Real and imaginary parts of the bottomonium ground state (Υ) binding energy as a function of p_{hard} . Both isotropic $\xi = 0$ and anisotropic $\xi = 1$ cases are shown. See text for parameters such as lattice size, lattice spacing, etc.

GeV. In Fig. 1 we show both the real part (black line with filled circles) and the imaginary part (red line with filled squares) of the isotropic ground state binding energy. Comparing these two curves, we see that the imaginary part of the binding energy becomes comparable to the real part at $p_{\text{hard}} \sim 1.63 T_c$. In contrast, in the anisotropic case ($\xi = 1$) we find that the intersection between the imaginary (blue line with open triangles) and real parts (green line with open diamonds) occurs at $p_{\text{hard}} \sim 1.88 T_c$. In the range between 1 and $3 T_c$ we obtain a slope of 4.9×10^{-2} GeV for the imaginary part of the binding energy when $\xi = 0$ and 6.4×10^{-2} GeV when $\xi = 1$. In the isotropic case Dumitru’s perturbative calculation [49] gives a slope of 8×10^{-2} GeV. Our method is non-perturbative since we don’t assume perturbations around Coulomb wave functions, so one should not be surprised to see some important differences.

In Fig. 2 we plot the binding energy of the bottomonium ground state (Υ) as a function of p_{hard} . For this figure, we used a lattice size of 256^3 with lattice dimension of $L = 25.6 \text{ GeV}^{-1}$ and a lattice spacing of $a = 0.1 \text{ GeV}^{-1}$. For the bottomonium mass, we used $m_b = 4.7 \text{ GeV}$. In Fig. 2 we show both the real part (black line with filled circles) and the imaginary part (red line with filled squares) of the isotropic ground state binding energy. When $\xi = 0$, we see that the imaginary part of the binding energy becomes comparable to the real part at $p_{\text{hard}} \sim 2.8 T_c$. In the anisotropic case ($\xi = 1$) we find that the intersection between the imaginary (blue line with open triangles) and real parts (green line with open diamonds) occurs at approximately $3.5 T_c$. For $\xi = 0$, in the range between 1 and $4 T_c$ we obtain a slope of 2.8×10^{-2} GeV for the imaginary part of the binding energy. In the anisotropic case ($\xi = 1$) we find a slope of 4.2×10^{-2} GeV. We can once again compare to the analytic result of Dumitru [49] which gives an isotropic slope of 5×10^{-2} for the Υ . Once again, the numbers are roughly in agreement.

In Fig. 3 we plot the binding energy of the first p-wave excited state of bottomonium (χ_b)

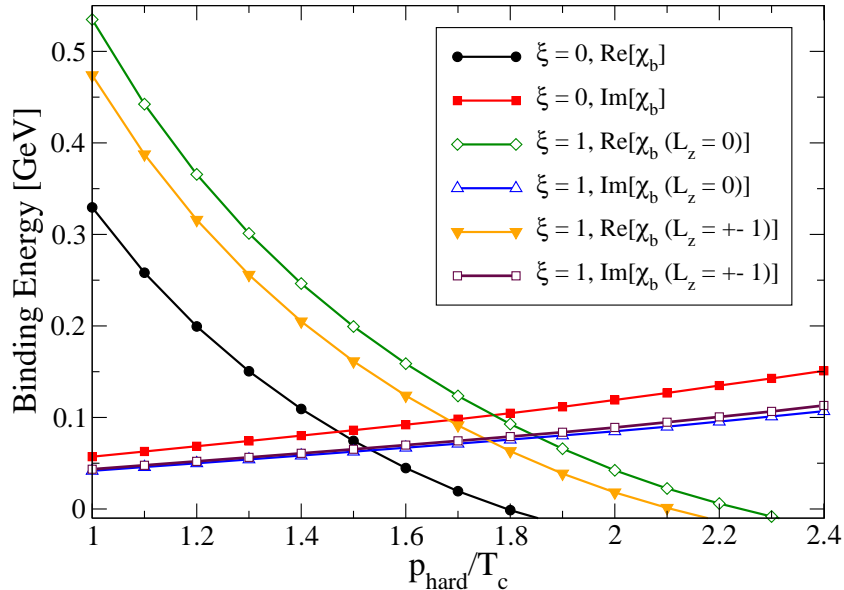


FIG. 3: Real and imaginary parts of χ_b binding energy as a function of p_{hard} . Both isotropic $\xi = 0$ and anisotropic $\xi = 1$ cases are shown. See text for parameters such as lattice size, lattice spacing, etc.

as a function of p_{hard} . For this figure we used a lattice size of 256^3 with lattice dimension of $L = 38.4 \text{ GeV}^{-1}$ and a lattice spacing of $a = 0.15 \text{ GeV}^{-1}$. For the bottomonium mass, we used $m_b = 4.7 \text{ GeV}$. As was the case with the bottomonium ground state we see an increase in the real part of the binding energy with increasing anisotropy. Most importantly, we find that there is an approximately 60 MeV splitting between the $L_z = 0$ and $L_z = \pm 1$ states with the states with $L_z = \pm 1$ having the lower binding energy. We would therefore expect fewer $L_z = \pm 1$ states of the χ_b to be produced in an anisotropic plasma. Determining precisely how many fewer would be produced requires knowledge of the time evolution of the momentum scale p_{hard} and anisotropy ξ .

B. Fixing number density or energy density

As mentioned in the beginning of this section, when one is working in a non-equilibrium setting it is necessary to specify which quantities are held fixed. In equilibrium, it is sufficient to specify the temperature. The temperature then uniquely determines the number density, energy density, etc. In the previous subsection we presented results obtained when one holds the hard momentum scale p_{hard} fixed while varying the anisotropy parameter ξ . Doing so, however, results in different number densities and energy densities for different anisotropies (ξ). Here we discuss how to fix either the number or energy density by adjusting p_{hard} appropriately. We first demonstrate this in the case of the number density and show that for small anisotropy the scalings required to fix the number density or energy density are practically identical. We then present results for the binding energies of the states we are interested in for the case of fixed number density, since in this paper we concentrate on anisotropies which are small enough that the difference between the cases of fixed number density and fixed energy density is numerically very small.

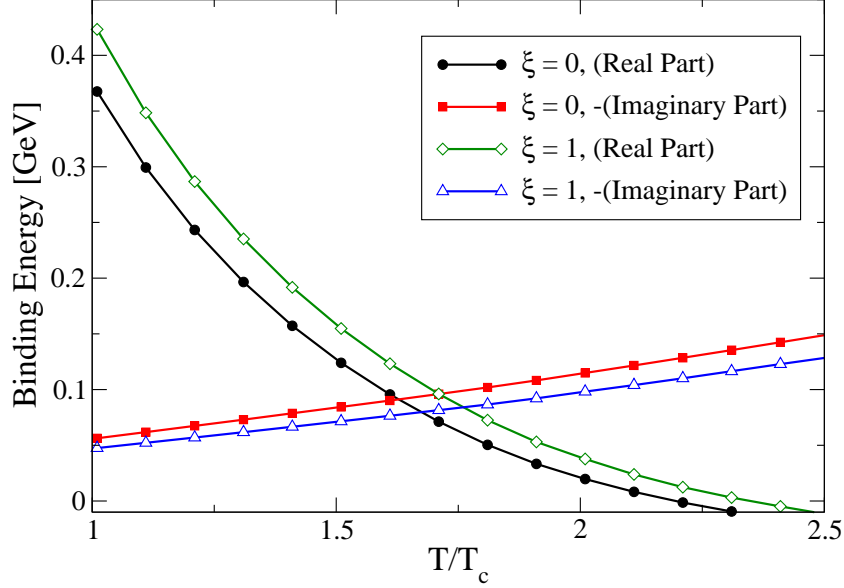


FIG. 4: Real and imaginary parts of the charmonium ground state (J/ψ) binding energy as a function of temperature assuming fixed number density. Both isotropic $\xi = 0$ and anisotropic $\xi = 1$ cases are shown. See text for parameters such as lattice size, lattice spacing, etc.

The number density as a function of ξ and p_{hard} can be calculated for an arbitrary isotropic distribution f_{iso} [52]

$$n(\xi, p_{\text{hard}}) = \frac{n_{\text{iso}}(p_{\text{hard}})}{\sqrt{1 + \xi}}, \quad (20)$$

where n_{iso} is the number density associated with the isotropic distribution function f_{iso} via

$$n_{\text{iso}}(p_{\text{hard}}) = \int \frac{d^3p}{(2\pi)^3} f_{\text{iso}}(|\mathbf{p}|, p_{\text{hard}}). \quad (21)$$

Since n_{iso} only contains one dimensionful scale, by dimensional analysis we have $n_{\text{iso}} \propto p_{\text{hard}}^3$. In order to keep the number density (20) fixed as one changes ξ , one can adjust p_{hard} by requiring

$$p_{\text{hard}} = (1 + \xi)^{1/6} T \quad [\text{fixed number density}], \quad (22)$$

where T is the corresponding isotropic scale (temperature) which gives the target number density when $\xi = 0$, i.e. $n_{\text{iso}}(T)$.

Similarly, the energy density as a function of ξ and p_{hard} can be calculated for an arbitrary isotropic distribution f_{iso} [64]

$$\mathcal{E}(\xi, p_{\text{hard}}) = \mathcal{R}(\xi) \mathcal{E}_{\text{iso}}(p_{\text{hard}}), \quad (23)$$

where \mathcal{E}_{iso} is the energy density associated with the isotropic distribution function f_{iso} and

$$\mathcal{R}(\xi) = \frac{1}{2} \left(\frac{1}{1 + \xi} + \frac{\arctan \sqrt{\xi}}{\sqrt{\xi}} \right). \quad (24)$$

Since \mathcal{E}_{iso} only contains one dimensionful scale, by dimensional analysis we have $\mathcal{E}_{\text{iso}} \propto p_{\text{hard}}^4$ and we can fix the energy density to the corresponding isotropic energy density with scale

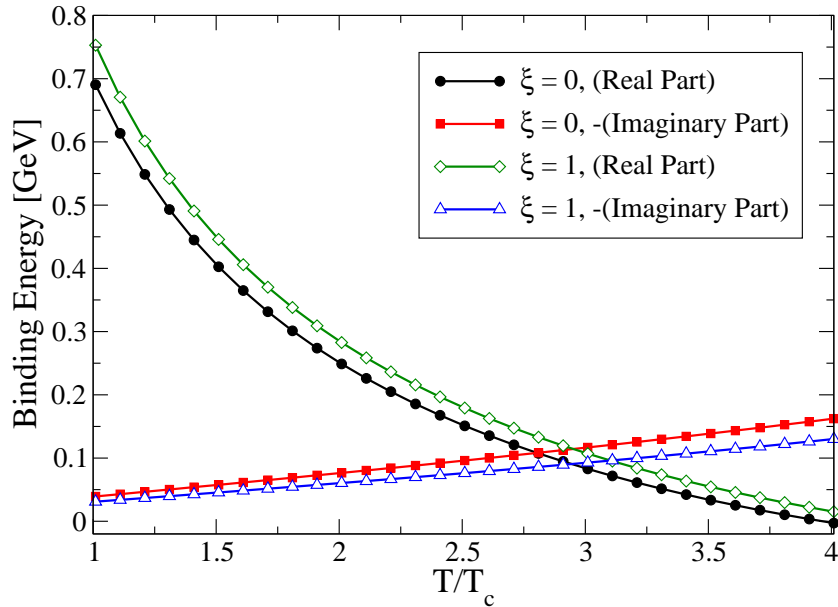


FIG. 5: Real and imaginary parts of bottomonium ground state (Υ) binding energy as a function of temperature assuming fixed number density. Both isotropic $\xi = 0$ and anisotropic $\xi = 1$ cases are shown. See text for parameters such as lattice size, lattice spacing, etc.

T by requiring

$$p_{\text{hard}} = T/[\mathcal{R}(\xi)]^{1/4} \quad [\text{fixed energy density}] . \quad (25)$$

The scalings for fixed number density (22) and fixed energy density (25) are different; however, in the limit of small anisotropies the scalings are very close. Expanding to quadratic order, one finds

$$\frac{p_{\text{hard}}}{T} = 1 + \frac{1}{6}\xi - \frac{29}{360}\xi^2 + \mathcal{O}(\xi^3) \quad [\text{fixed number density}] , \quad (26a)$$

$$\frac{p_{\text{hard}}}{T} = 1 + \frac{1}{6}\xi - \frac{5}{72}\xi^2 + \mathcal{O}(\xi^3) \quad [\text{fixed energy density}] , \quad (26b)$$

which agree at linear order and differ by 7.4% in the quadratic coefficient. One finds that, when including all orders in the expansion, the right hand sides of (26a) and (26b) differ by only 0.25% at $\xi = 1$. Therefore, for the range of anisotropies considered here, the two scalings are functionally equivalent. We will therefore only present results for fixed number density with the understanding that the fixed energy density results are indistinguishable by the human eye.

In Figs. 4, 5, and 6, we show the binding energies which result from the fixed number density rescaling of the horizontal axes of Figs. 1, 2, and 3. As can be seen from Figs. 4, 5, and 6, requiring fixed number/energy density weakens the effect of anisotropies on the ground state binding energies. In the case of the ground states of charmonium and bottomonium shown in Figs. 4 and 5 we find that the splitting between the $\xi = 0$ and $\xi = 1$ cases at the critical temperature is approximately 50 MeV in both cases.

Finally, we emphasize that in the case of the first excited states of bottomonium shown in Fig. 6 the splitting between the $L_z = 0$ and $L_z = \pm 1$ states is unaffected by the rescaling since we have $\xi = 1$ for both states. Therefore, one has a relatively clean observable that

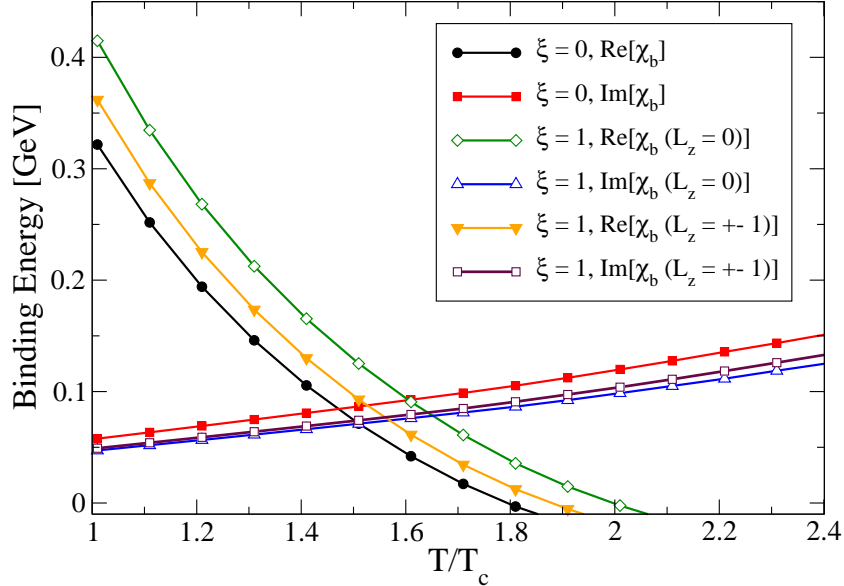


FIG. 6: Real and imaginary parts of the χ_b binding energy as a function of temperature assuming fixed number density. Both isotropic $\xi = 0$ and anisotropic $\xi = 1$ cases are shown. See text for parameters such as lattice size, lattice spacing, etc.

is sensitive to plasma anisotropies regardless of the quantity which is assumed to be held fixed.

V. CONCLUSIONS

In this paper we have presented first results on the effect of including both the real and imaginary parts of the heavy quarkonium potential on the binding energies of the charmonium ground state (J/ψ), the bottomonium ground state (Υ), and the first p -wave excited state of bottomonium (χ_b). We did this by numerically solving the three-dimensional Schrödinger equation for the complex potential given by Eqs. (4) and (6). This enabled us to extract both the real and imaginary parts of the binding energies for the states. Using our model potential, we investigated both isotropic and weakly anisotropic plasmas. We found that, there can be a sizable effect of momentum-space anisotropy on both the real and imaginary parts of the quarkonium binding energy. One can estimate the disassociation temperature of the states by determining the temperature at which the real and imaginary parts of the binding energy become the same. Using this criteria, in the isotropic case we estimate the J/ψ , Υ and χ_b to have disassociation temperatures of $1.6 T_c$, $2.8 T_c$, and $1.5 T_c$, respectively. We note, however, that even prior to these disassociation temperatures the states will be suppressed due to the exponential decay of the states with a rate related to the imaginary part of the binding energy. We plan to investigate the phenomenological impact of our results on the time evolution of quarkonium decay in a future publication.

In the case of a plasma with a finite momentum-space anisotropy, we presented results for both fixed hard momentum scale and fixed number density. Our results demonstrate that the corresponding anisotropic states have a higher binding energy in accordance with previous results that employed only the real part of the quarkonium potential used herein [35]. We

showed that, for small anisotropy, fixing the number density and fixing the energy density gives results which are the same to within less than a fraction of a percent. We demonstrated that fixing the number density reduces the effect of anisotropy compared to the case of fixing the hard momentum scale, but does not completely remove the effect of momentum-space anisotropy on the binding energies. Finally, we emphasized the importance of the finite-anisotropy splitting between the χ_b states with $L_z = 0$ and $L_z = \pm 1$. This splitting is independent of whether one fixes the hard momentum scale, number density, or energy density. Therefore, this splitting represents a possible observable which could be used to determine the time-averaged plasma anisotropy parameter.

Looking forward, to fully assess the phenomenological impact of plasma momentum-space anisotropies on quarkonium states requires the convolution of the results presented here with the space-time evolution of the hard momentum scale and anisotropy parameter. A method for determining the dynamical evolution of these parameters has recently been determined [47, 48]. In addition, since these works show that ξ can become large, it will be necessary to investigate the effect of large anisotropies on quarkonium binding energies. The calculations necessary to address these questions are currently underway.

Acknowledgments

We thank A. Dumitru for discussions. K. McCarty was supported during the summer of 2010 by the Cormack Fund. M. Strickland was supported in part by the Helmholtz International Center for FAIR Landesoffensive zur Entwicklung Wissenschaftlich-Ökonomischer Exzellenz program.

Note added

In arXiv versions 1-3 there was a mistake in the final results for the imaginary part of the binding energies. The mistake stems from the fact that we had subtracted the full complex-valued potential at infinity V_∞ ; however, formally only the real part of V_∞ should be subtracted since the imaginary part of V_∞ is related to heavy quark damping in the plasma which is physically relevant. As a consequence all imaginary parts of the binding energies are changed and we have updated all figures. While the results are qualitatively similar, the key change is that the imaginary part of the binding energy now has a stronger dependence on the anisotropy parameter, ξ , in most cases.

Appendix A: Numerical Tests

1. Convergence Test

In this appendix we present some convergence data for a particular state in order to demonstrate the approach to the continuum limit. In Fig. 7 we show both the real and imaginary parts of the bottomonium ground state binding energy for three different lattice spaces of 128^3 , 256^3 , and 512^3 . For each of the runs, the lattice size was fixed to $L = 25.6$ GeV^{-1} with the lattice spacing in each case given by $a = 0.2$, $a = 0.1$, and $a = 0.05$ GeV^{-1} ,

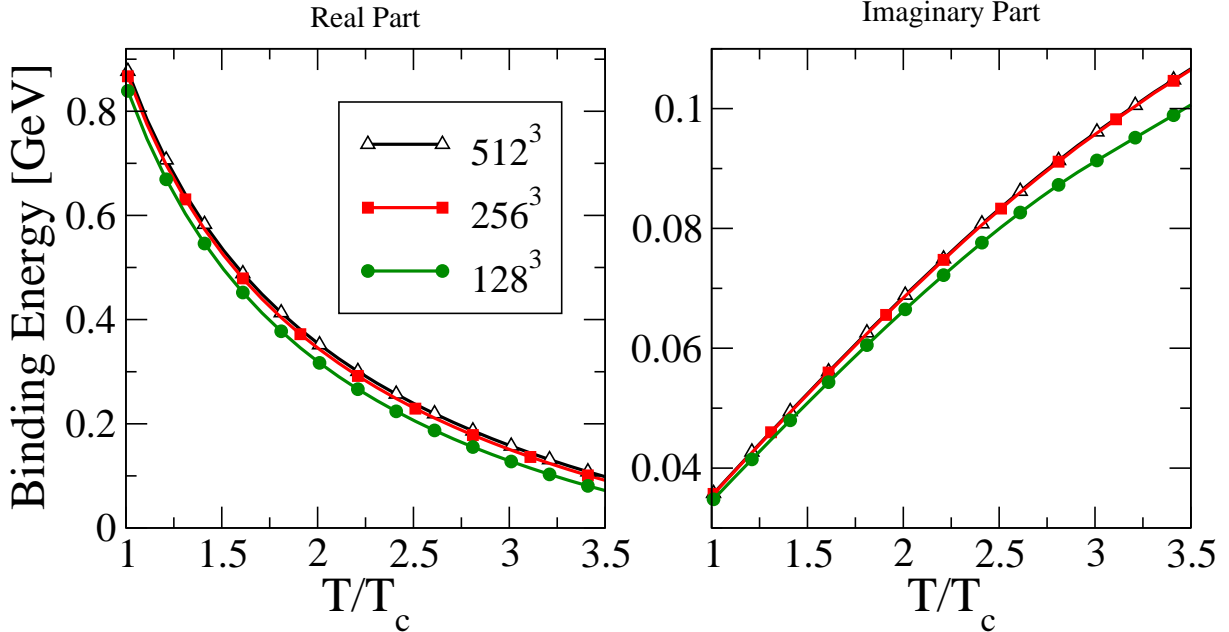


FIG. 7: Real and imaginary parts of the bottomonium binding energy for three different lattice sizes of 128^3 , 256^3 , and 512^3 .

respectively. We chose $\xi = 1$, $m_b = 4.7$ GeV and used an imaginary-time step given by $\Delta\tau = a^2/8$ in each case.

As can be seen from this figure, there is a larger effect due to reducing the lattice space on the real part than the imaginary part. This is to be expected since the real part contains a divergence at the origin, whereas the imaginary part is regular. In the case of the real part at $3 T_c$, we see an approximately 8.0% correction when going from 128^3 to 256^3 and a 2.6% correction when going from 256^3 to 512^3 . The corrections in the case of the imaginary part are 2.4% and 0.16%, respectively. Therefore we see that the 256^3 runs presented in the body of the text are reliable up to corrections on the order of 3%.

2. Harmonic Oscillator with complex spring constant

In this part of the appendix we explore the ability of the FDTD algorithm to handle the case of complex potentials. We investigate a simple one dimensional test case which consists of solving the Schrödinger equation for a particle of mass m in a harmonic oscillator potential which has a complex spring constant k . We first derive the analytic solution and then compare the output of the code and the analytic solution.

Our goal is to solve the time-independent Schrödinger equation for a particle of mass m which is bounded by the quadratic potential $V(x) = kx^2/2$, in the case that k is complex. Before proceeding, we review the solution in the case that k is real, writing it first in terms of Parabolic Cylinder Functions and then showing how these reduce to the Hermite Polynomials.

a. *Review of the case of a real spring constant*

We are interested in solving the time independent 1D Schrödinger equation for the harmonic oscillator potential

$$-\frac{\hbar^2}{2m} \frac{d^2\psi}{dx^2} + \frac{k}{2} x^2 \psi = E\psi. \quad (\text{A1})$$

To begin with, we introduce the variables $\omega \equiv \sqrt{\frac{k}{m}}$, $\alpha \equiv \left(\frac{mk}{\hbar^2}\right)^{1/4}$, $\lambda \equiv \frac{2E}{\hbar\omega}$, and $u \equiv \alpha x$ which allow us to write (A1) compactly as

$$\frac{d^2\psi}{du^2} - (u^2 - \lambda)\psi = 0. \quad (\text{A2})$$

b. *Asymptotic Behavior*

We now want to find solutions for our wavefunction at $|u| \rightarrow \infty$. In the limit $|u| \gg 1$ Eq. (A2) becomes

$$\lim_{|u| \rightarrow \infty} \frac{d^2\psi}{du^2} = u^2\psi, \quad (\text{A3})$$

which has an asymptotic solutions of the form

$$\lim_{|u| \rightarrow \infty} \psi(u) = A u^p e^{-u^2/2}, \quad (\text{A4})$$

or

$$\lim_{|u| \rightarrow \infty} \psi(u) = B u^q e^{u^2/2}, \quad (\text{A5})$$

with A and B being arbitrary constants. Since ψ must remain finite as $|u| \rightarrow \infty$, this requires that we discard the second solution. Requiring that the wavefunction be single valued for negative u implies that p must be an integer.³ This yields an asymptotic solution of the form

$$\lim_{|u| \rightarrow \infty} \psi(u) = A u^p e^{-u^2/2}, \quad (\text{A6})$$

where p is integer-valued.

c. *Solution in terms of Parabolic Cylinder Functions*

We now define new variables $a = -\lambda/2$ and $b = \sqrt{2}u$ such that $u^2 = b^2/2$ and $2 d^2/db^2 = d^2/du^2$. Substituting these into Eq. (A2) gives

$$\frac{d^2\psi}{db^2} - \left(\frac{1}{4}b^2 + a\right) \psi = 0. \quad (\text{A7})$$

The solution to this differential equation is given by the Parabolic Cylinder Function D from Chapter 19 of Abramowitz and Stegun [65] $\psi(a, b) = U(a, b) = D_{-a-\frac{1}{2}b}(b)$. If $U(a, b)$ is a

³ Note that one could move the cut along the negative u axis into the complex plane, so the more properly-stated requirement is that the wavefunction be single-valued everywhere in the complex plane.

solution, then so are $U(a, -b)$, $U(-a, ib)$, and $U(-a, -ib)$. This leaves us with the general solution

$$\psi(u) = AU\left(-\frac{\lambda}{2}, \sqrt{2}u\right) + BU\left(\frac{\lambda}{2}, i\sqrt{2}u\right). \quad (\text{A8})$$

d. Matching Asymptotic Behavior

Now we analyze the asymptotic behavior of U when $b \gg a$. For $b \gg a$, we have [65]

$$U(a, b) \sim e^{-\frac{1}{4}b^2} b^{-a-\frac{1}{2}} (1 - \mathcal{O}(b^{-2})). \quad (\text{A9})$$

We see that in the limit $b \rightarrow \infty$ that $U(a, ib)$ approaches $+\infty$. Since the wavefunction should be finite at $b \rightarrow \infty$ this requires $B = 0$ in Eq. (A8). We can solve for λ by matching to the asymptotic form given in Eq. (A6)

$$\left(-\frac{\lambda}{2} + \frac{1}{2}\right) = -p. \quad (\text{A10})$$

where p must be an integer as discussed previously. Solving for λ gives us $\lambda = 2p + 1$, which tells us that λ is discrete. This leaves us with the solution to the quantum harmonic oscillator differential equation in terms of Parabolic Cylinder D functions

$$\psi(u) = AU\left(-\frac{2p+1}{2}, \sqrt{2}u\right). \quad (\text{A11})$$

e. Connection to Hermite Polynomials

When n is a non-negative integer, $U(-n - 1/2, b)$ is expressible in terms of Hermite Polynomials [65]

$$U(-n - 1/2, b) = 2^{-\frac{1}{2}n} e^{-\frac{1}{4}b^2} H_n\left(\frac{b}{\sqrt{2}}\right), \quad (\text{A12})$$

where $H_n(x)$ is a Hermite polynomial. Using this we find that Eq. (A11) can be expressed as

$$\psi_p(u) = A_p e^{-\frac{1}{2}u^2} H_p(u). \quad (\text{A13})$$

This is the standard textbook form of the quantum harmonic oscillator wavefunctions. We now extend the general solution (A8) to the case where k can be complex.

3. Extending the solution to the case of a complex spring constant

We now examine the behavior of our solution when the spring constant k is complex. To begin, we note a symmetry of Eq. (A2): namely, if we find that a solution for a given k is given by ψ , then the solution for the complex conjugate spring constant k^* will be given by ψ^* . Therefore, it suffices to solve the equation in only half of the complex k plane. In order to find the specific solution, we take the general solution in Eq. (A8) and re-examine its asymptotic behavior. Depending on the angle of k in the complex plane, we find that one

needs to set either A or B in Eq. (A8) to zero. For large values of $u \gg |a|$ we have from Ref. [65]

$$U(a, u) \sim e^{-\frac{1}{4}u^2} u^{-a-\frac{1}{2}}, \quad (\text{A14})$$

where we have dropped a factor of $\sqrt{2}$ for simplicity. For complex-valued $u = \beta + i\gamma$ with real-valued β and γ , we have three cases that determine the asymptotic convergence of $U(a, u)$: $\beta > \gamma$, $\beta < \gamma$, and $\beta = \gamma$.

a. Case A: Real part greater than imaginary part ($\beta > \gamma$)

In this case, we must require $B = 0$ in Eq. (A8) and we have

$$\begin{aligned} \psi(u) = U(a, \beta + i\gamma) &\sim e^{-\frac{1}{4}(\beta+i\gamma)^2} u^{-a-\frac{1}{2}} \\ &= e^{-\frac{1}{4}(\beta^2+2i\beta\gamma-\gamma^2)} u^{-a-\frac{1}{2}} \\ &= e^{-\frac{1}{4}\beta^2} e^{-\frac{1}{2}i\beta\gamma} e^{\frac{1}{4}\gamma^2} u^{-a-\frac{1}{2}}, \end{aligned} \quad (\text{A15})$$

which converges since $\beta > \gamma$.

b. Case B: Real part less than imaginary part ($\beta < \gamma$)

In this case, we require $A = 0$ in Eq. (A8) and we have

$$\begin{aligned} U(-a, iu) &= U(-a, i\beta - \gamma) \\ &\sim e^{-\frac{1}{4}(i\beta-\gamma)^2} u^{a-\frac{1}{2}} \\ &= e^{-\frac{1}{4}(-\beta^2-2i\beta\gamma+\gamma^2)} u^{a-\frac{1}{2}} \\ &= e^{\frac{1}{4}\beta^2} e^{+\frac{1}{2}i\beta\gamma} e^{-\frac{1}{4}\gamma^2} u^{a-\frac{1}{2}}, \end{aligned} \quad (\text{A16})$$

which converges since $\beta < \gamma$.

c. Case C: Real part equal to imaginary part ($\beta = \gamma$)

In this case, the solution diverges; however, as we will show below, $\beta = \gamma$ corresponds to a purely repulsive potential so one could expect such singular behavior. Since here $\beta = \gamma$, we can rewrite

$$u = \beta + i\beta = |u|e^{i\pi/4}. \quad (\text{A17})$$

Also, since $u = (mk/\hbar^2)^{1/4}x$ and $k = |k|e^{i\theta}$, we have

$$u = k^{1/4}(m/\hbar^2)^{1/4}x \quad (\text{A18})$$

$$= e^{i\theta/4}(m|k|/\hbar^2)^{1/4}x \quad (\text{A19})$$

Equating the imaginary parts of Equations (A17) and (A19), we have

$$e^{i\pi/4} = e^{i\theta/4} \quad (\text{A20})$$

which means $\theta = \pi$ and $k = -1|k|$. This corresponds to a repulsive spring constant which has no bound solutions.

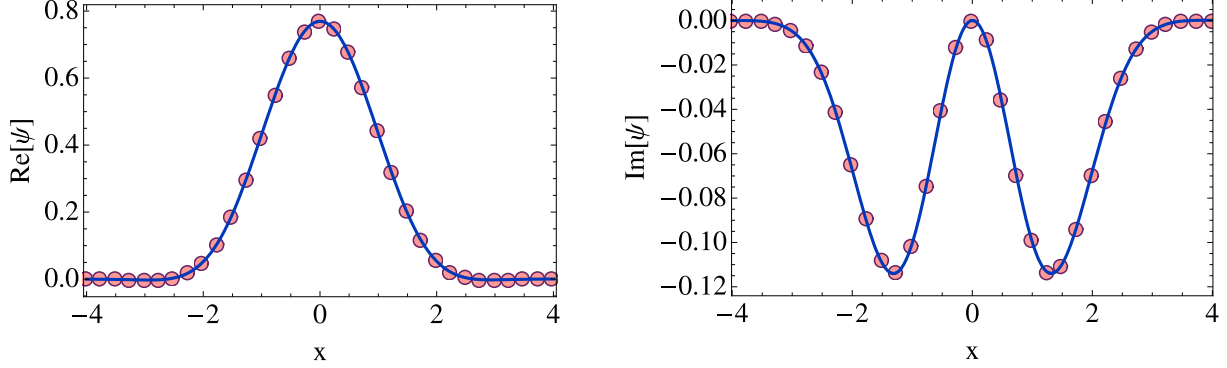


FIG. 8: Plot showing real and imaginary parts of the wavefunction for a complex harmonic oscillator potential with $k = 1 + i$. The solid lines are the analytic results and the circles are sampled points obtained from the numerical solution using the FDTD method [63].

4. Comparison of Numerical Solution and Analytic Solution

In this section, we will examine two different complex values of k . Since $u = \alpha x$ where $\alpha = (mk/\hbar^2)^{1/4}$, the solution depends on the real and imaginary parts of the spring constant k . This determines whether $A = 0$ or $B = 0$ in Eq. (A8) as discussed above. Below, we use natural units with $\hbar = c = 1$ and take $m = 1$ GeV.

a. Case $k = 1 + i$

In this case, we have $k = e^{i\pi/4}|k|$ and $u = e^{i\pi\theta/16}u_r$ where $u_r = (m|k|/\hbar^2)^{1/4}x$. Therefore, $\beta > \gamma$ and we must use case A. The solution becomes

$$\psi(u) = AU \left(-\frac{\lambda}{2}, \sqrt{2}u \right). \quad (\text{A21})$$

In Fig. 8 we plot the result for the ground state which corresponds to $\lambda = 1$ with the constant A fixed to require a normalized wavefunction. The solid lines are the analytic results and the circles are sampled points obtained from numerical solution using the FDTD method [63].⁴ As we can see from this figure, the FDTD algorithm is able to obtain very good agreement in both the real and imaginary parts of the wavefunction. We can also compare the ground state energy predicted analytically by Eq. (A21) which is $E_0 = 0.549342 + 0.227545i$ with the FDTD algorithm's result. The FDTD algorithm, using 200 points distributed with a step size of 0.05 and a convergence tolerance of 10^{-8} , gives $E_0 = 0.549251 + 0.227479i$, which represents an accuracy of approximately 0.01%.

⁴ The wavefunction can be rotated by an arbitrary complex phase $e^{i\phi}$ without affecting the probability amplitudes. In practice, the code converges to a different random phase angle during each run. In order to compare to the analytic results for the real and imaginary parts of the wavefunction we manually rotate the numerically determined wavefunctions such that $\text{Im}[\psi(x=0)] = 0$.

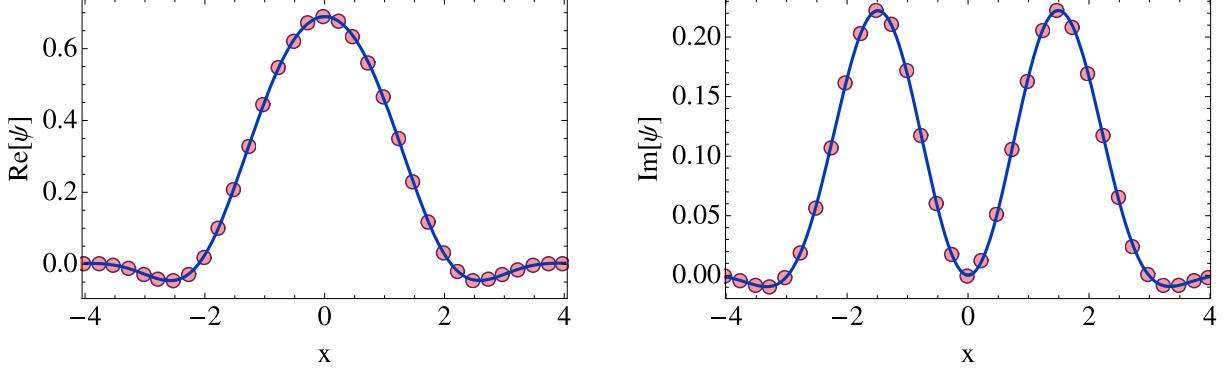


FIG. 9: Plot showing real and imaginary parts of the wavefunction for a complex harmonic oscillator potential with $k = -i$. The solid lines are the analytic results and the circles are sampled points obtained from numerical solution using the FDTD method [63].

b. Case $k = -i$

In this case, we have $k = e^{i3\pi/2}|k|$ and $u = e^{i3\pi\theta/8}u_r$ where $u_r = (m|k|/\hbar^2)^{1/4}x$. Therefore, $\beta < \gamma$ and we must use case B. The solution becomes

$$\psi(u) = BU \left(\frac{\lambda}{2}, i\sqrt{2}u \right). \quad (\text{A22})$$

In Fig. 9 we plot the result for the ground state which corresponds to $\lambda = 1$ with B fixed to require a normalized wavefunction. The solid lines are the analytic results and the circles are sampled points obtained from numerical solution using the FDTD method [63]. As we can see from this figure, the FDTD algorithm is able to obtain very good agreement in both the real and imaginary parts of the wavefunction. We can also compare the ground state energy predicted analytically by Eq. (A22) which is $E_0 = 0.353553 - 0.353553i$ with the FDTD algorithm's result. The FDTD algorithm, using 200 points distributed with step size of 0.05 and a convergence tolerance of 10^{-8} , gives $E_0 = 0.353522 - 0.353478i$, which represents an accuracy of approximately $5 \times 10^{-3} \%$.

The results of the two cases presented in this appendix show that the FDTD algorithm is able to obtain accurate wavefunctions and eigenvalues even in the case that the potential is complex-valued. The agreement between the analytic and numerical results can be improved by using finer lattice spacings and larger number of points.

-
- [1] E. V. Shuryak, Phys. Rept. **61**, 71 (1980).
 - [2] D. J. Gross, R. D. Pisarski, and L. G. Yaffe, Rev. Mod. Phys. **53**, 43 (1981).
 - [3] W. Lucha, F. F. Schoberl, and D. Gromes, Phys. Rept. **200**, 127 (1991).
 - [4] E. Eichten, K. Gottfried, T. Kinoshita, K. D. Lane, and T.-M. Yan, Phys. Rev. **D21**, 203 (1980).
 - [5] N. Brambilla, A. Pineda, J. Soto, and A. Vairo, Rev. Mod. Phys. **77**, 1423 (2005), hep-ph/0410047.
 - [6] T. Matsui and H. Satz, Phys. Lett. **B178**, 416 (1986).

- [7] F. Karsch, M. T. Mehr, and H. Satz, *Z. Phys.* **C37**, 617 (1988).
- [8] A. Mocsy and P. Petreczky, *Eur. Phys. J.* **C43**, 77 (2005), hep-ph/0411262.
- [9] C.-Y. Wong, *Phys. Rev.* **C72**, 034906 (2005), hep-ph/0408020.
- [10] A. Mocsy and P. Petreczky, *Phys. Rev.* **D73**, 074007 (2006), hep-ph/0512156.
- [11] D. Cabrera and R. Rapp, *Phys. Rev.* **D76**, 114506 (2007), hep-ph/0611134.
- [12] A. Mocsy and P. Petreczky, *Phys. Rev. Lett.* **99**, 211602 (2007), 0706.2183.
- [13] W. M. Alberico, A. Beraudo, A. De Pace, and A. Molinari, *Phys. Rev.* **D77**, 017502 (2008), 0706.2846.
- [14] A. Mocsy and P. Petreczky, *Phys. Rev.* **D77**, 014501 (2008), 0705.2559.
- [15] A. Mocsy (2008), 0811.0337.
- [16] T. Umeda, K. Nomura, and H. Matsufuru, *Eur. Phys. J.* **C39S1**, 9 (2005), hep-lat/0211003.
- [17] M. Asakawa and T. Hatsuda, *Phys. Rev. Lett.* **92**, 012001 (2004), hep-lat/0308034.
- [18] S. Datta, F. Karsch, P. Petreczky, and I. Wetzorke, *Phys. Rev.* **D69**, 094507 (2004), hep-lat/0312037.
- [19] G. Aarts et al., *PoS LAT2006*, 126 (2006), hep-lat/0610065.
- [20] T. Hatsuda, *PoS LAT2006*, 010 (2006).
- [21] A. Jakovac, P. Petreczky, K. Petrov, and A. Velytsky, *Phys. Rev.* **D75**, 014506 (2007), hep-lat/0611017.
- [22] T. Umeda, *Phys. Rev.* **D75**, 094502 (2007), hep-lat/0701005.
- [23] G. Aarts, C. Allton, M. B. Oktay, M. Peardon, and J.-I. Skullerud, *Phys. Rev.* **D76**, 094513 (2007), 0705.2198.
- [24] G. Aarts et al. (2010), 1010.3725.
- [25] Y. Nakahara, M. Asakawa, and T. Hatsuda, *Phys.Rev.* **D60**, 091503 (1999), hep-lat/9905034.
- [26] M. Asakawa, T. Hatsuda, and Y. Nakahara, *Prog.Part.Nucl.Phys.* **46**, 459 (2001), hep-lat/0011040.
- [27] M. Asakawa, T. Hatsuda, and Y. Nakahara, *Nucl.Phys.* **A715**, 863 (2003), hep-lat/0208059.
- [28] N. Armesto et al., *J. Phys.* **G35**, 054001 (2008), 0711.0974.
- [29] R. Rapp, D. Blaschke, and P. Crochet (2008), 0807.2470.
- [30] M. Laine, O. Philipsen, P. Romatschke, and M. Tassler, *JHEP* **03**, 054 (2007), hep-ph/0611300.
- [31] M. Laine, *JHEP* **05**, 028 (2007), 0704.1720.
- [32] A. Beraudo, J. P. Blaizot, and C. Ratti, *Nucl. Phys.* **A806**, 312 (2008), 0712.4394.
- [33] N. Brambilla, J. Ghiglieri, A. Vairo, and P. Petreczky, *Phys. Rev.* **D78**, 014017 (2008), 0804.0993.
- [34] A. Dumitru, Y. Guo, and M. Strickland, *Phys. Lett.* **B662**, 37 (2008), 0711.4722.
- [35] A. Dumitru, Y. Guo, A. Mocsy, and M. Strickland, *Phys. Rev.* **D79**, 054019 (2009), 0901.1998.
- [36] Y. Burnier, M. Laine, and M. Vepsalainen (2009), 0903.3467.
- [37] A. Dumitru, Y. Guo, and M. Strickland, *Phys. Rev.* **D79**, 114003 (2009), 0903.4703.
- [38] J. Noronha and A. Dumitru, *Phys.Rev.* **D80**, 014007 (2009), 0903.2804.
- [39] O. Philipsen and M. Tassler (2009), 0908.1746.
- [40] W. Israel, *Ann. Phys.* **100**, 310 (1976).
- [41] W. Israel and J. M. Stewart, *Ann. Phys.* **118**, 341 (1979).
- [42] G. Baym, *Phys. Lett.* **B138**, 18 (1984).
- [43] A. Muronga, *Phys. Rev. Lett.* **88**, 062302 (2002), nucl-th/0104064.
- [44] A. Muronga, *Phys. Rev.* **C69**, 034903 (2004), nucl-th/0309055.
- [45] M. Martinez and M. Strickland, *Phys. Rev.* **C79**, 044903 (2009), 0902.3834.

- [46] W. Florkowski and R. Ryblewski (2010), 1007.0130.
- [47] M. Martinez and M. Strickland, Nucl. Phys. **A848**, 183 (2010), 1007.0889.
- [48] M. Martinez and M. Strickland (2010), 1011.3056.
- [49] A. Dumitru (2010), 1010.5218.
- [50] P. Romatschke and M. Strickland, Phys. Rev. **D68**, 036004 (2003), hep-ph/0304092.
- [51] S. Mrowczynski, A. Rebhan, and M. Strickland, Phys. Rev. **D70**, 025004 (2004), hep-ph/0403256.
- [52] P. Romatschke and M. Strickland, Phys. Rev. **D70**, 116006 (2004), hep-ph/0406188.
- [53] B. Schenke and M. Strickland, Phys. Rev. **D74**, 065004 (2006), hep-ph/0606160.
- [54] M. Asakawa, S. A. Bass, and B. Muller, Prog. Theor. Phys. **116**, 725 (2007), hep-ph/0608270.
- [55] M. Laine, O. Philipsen, and M. Tassler, JHEP **09**, 066 (2007), 0707.2458.
- [56] O. Kaczmarek, F. Karsch, F. Zantow, and P. Petreczky, Phys. Rev. **D70**, 074505 (2004), hep-lat/0406036.
- [57] J. O. Andersen, L. E. Leganger, M. Strickland, and N. Su, Phys. Lett. **B696**, 468 (2011), 1009.4644.
- [58] J. O. Andersen, L. E. Leganger, M. Strickland, and N. Su (2011), 1103.2528.
- [59] J. O. Andersen, M. Strickland, and N. Su, JHEP **08**, 113 (2010), 1005.1603.
- [60] J. O. Andersen, M. Strickland, and N. Su, Phys. Rev. Lett. **104**, 122003 (2010), 0911.0676.
- [61] J. Noronha and A. Dumitru, Phys.Rev.Lett. **103**, 152304 (2009), 0907.3062.
- [62] I. Sudiarta and D. Geldart, Journal of Physics **A40**, 1885 (2007).
- [63] M. Strickland and D. Yager-Elorriaga, J. Comput. Phys. **229**, 6015 (2010), 0904.0939.
- [64] M. Martinez and M. Strickland, Phys. Rev. **C78**, 034917 (2008), 0805.4552.
- [65] M. Abramowitz and I. A. Stegun, *Handbook of Mathematical Functions with Formulas, Graphs, and Mathematical Tables* (Dover, New York, 1964), ninth dover printing, tenth gpo printing ed.